

Adaptive Transceiver Design for High-capacity Multi-modal Free-space Optical Communications with Commercial Devices and Atmospheric Turbulence

Zhouyi Hu, *Member, IEEE*, Zhaozhong Chen, Yiming Li, David M. Benton, Abdallah A. I. Ali, Mohammed Patel, Martin P.J. Lavery, Andrew D. Ellis, *Fellow, Optica*

(*Top-Scored Paper*)

Abstract—In this paper, to achieve higher robustness against atmospheric turbulence for high-capacity free-space optical (FSO) communications, an adaptive multi-modal FSO transceiver has been designed and experimentally demonstrated. We show that based on the dynamically estimated channel state information, modulation formats and power for different transmit modes can be adaptively allocated at the transmitter side. Meanwhile, at the receiver side, we show that the most suitable multi-input/multi-output decoder can be selected and employed to meet the requirement of forward error correction at the minimal expense of power consumption. By employing time-division multiplexed transmitter and receiver emulation and a spatial light modulator for turbulence emulation, an aggregate data rate of 590 Gbit/s/wavelength has been achieved when suffering from strong atmospheric turbulence, verifying the feasibility of the proposed adaptive transceiver over a turbulent FSO link. Moreover, to demonstrate practical applicability, all key devices such as transponder, multiplexer, and demultiplexer are commercially available in this work.

Index Terms—Atmospheric turbulence, free-space optics (FSO), mode-division multiplexing (MDM), multiple-input multiple-output (MIMO), optical wireless communication.

I. INTRODUCTION

The demand for internet traffic, which is currently attributed to the increasing popularity of 5G services, big data, cloud

Manuscript received xx xx, 2022. Research supported by EPSRC under grant number EP/T009047/1, EP/T009012/1, EP/S003436/1, EP/S016171/1, and the European Union’s Horizon 2020 research and innovation programme under the Marie Skłodowska-Curie grant agreement No. 713694 (Corresponding authors: Zhaozhong Chen, Yiming Li).

Z. Hu, Y. Li, D. Benton, M. Patel, and A. Ellis are with Aston Institute of Photonic Technology, Aston University, Birmingham, B4 7ET, UK (e-mail: z.hu6@aston.ac.uk; y.li70@aston.ac.uk; d.benton@aston.ac.uk; m.patel70@aston.ac.uk; andrew.ellis@aston.ac.uk).

Z. Chen, and M. Lavery are with James Watt school of engineering, University of Glasgow, Glasgow, G12 8QQ, UK (e-mail: Zhaozhong.Chen@glasgow.ac.uk; Martin.Lavery@glasgow.ac.uk).

A. Ali was with Aston University. He is now with Lumensisty Ltd, Unit 7, The Quadrangle, Abbey Park Industrial Estate, Romsey SO51 9DL, UK (e-mail: abdallah.ali@lumenisty.com).

computing, etc., keeps growing globally. To cope with this challenge, optical communications have been widely developed, where the current deployments are mainly based on fiber optics. However, it is not always economical to deploy optical fibers, for instance, in sparsely populated rural areas [1], [2]. Free-space optical (FSO) communication is a promising solution for its higher flexibility and cost-effectiveness in these scenarios. The FSO system offers significant advantages of data rate, security, power consumption, and licensed spectrum over its radio frequency competitor [3], [4]. Thus, FSO communication has been widely studied for many different applications from short reach (e.g., chip-to-chip communications) to long haul (e.g., satellite-to-ground communications) [5], although at the highest capacities, atmospheric turbulence still induces significant capacity outages [6]. Besides turbulence, other major limitations preventing FSO systems from achieving a higher data rate and longer transmission distance in practical applications include the increased atmospheric attenuation under various weather conditions and the limited launch power due to laser safety [7].

To overcome the optical network “capacity crunch”, leveraging parallel spatial paths, i.e., space-division multiplexing, is considered the only option by some researchers [8]. Specifically, for the FSO system, the capacity can be significantly boosted by modulating data on different spatial modes, e.g., orbital angular momentum (OAM) modes, Laguerre-Gaussian (LG) modes, and Hermite-Gaussian (HG) modes, among which OAM is widely studied [9]-[12]. OAM sacrifices its radial degrees of freedom in exchange for optical turbulence resilience. For a given aperture size, complete orthogonal basis sets can provide higher system capacity [13]-[15], but are potentially more sensitive to atmospheric turbulence, which not only induces intensity fluctuation but also additional inter-mode crosstalk [16]-[18]. Therefore, to implement the highest-capacity multi-mode FSO communication by leveraging complete modal basis sets, it is crucial to find a suitable solution to mitigate the impact of turbulence.

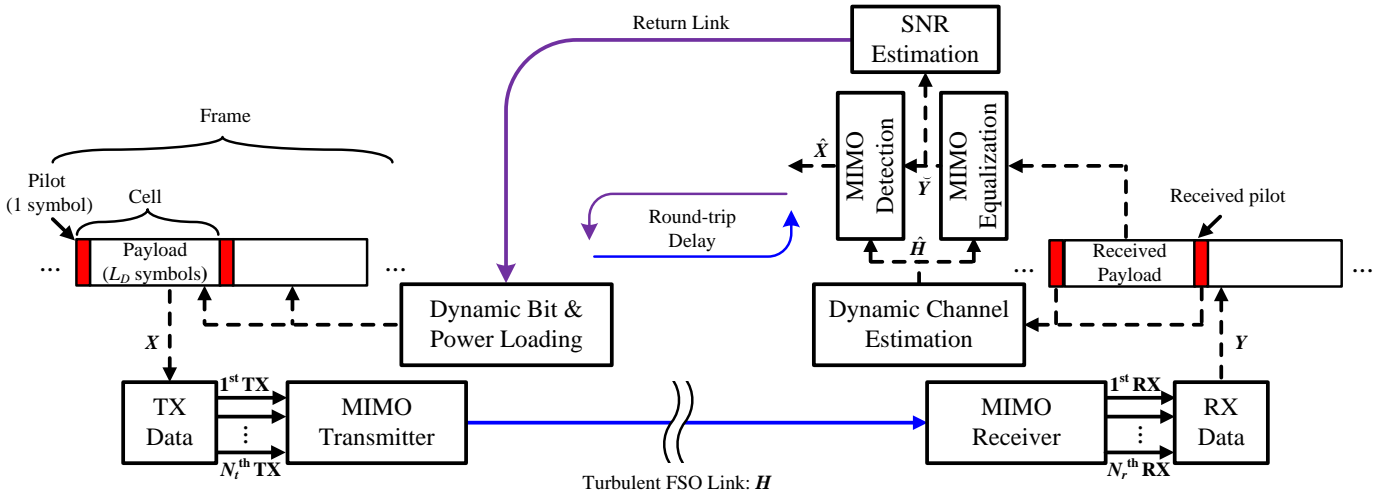


Fig. 1. Schematic diagram of the adaptive transceiver for FSO MIMO systems in atmospheric turbulence.

There are several potential solutions to mitigate atmospheric turbulence effects. The scheme based on adaptive optics (AO) is an efficient approach that has been widely studied due to its ability to correct wavefront distortions caused by atmospheric turbulence [7], [19]-[21]. It is particularly useful for the mode-division multiplexed (MDM) FSO systems in turbulence since the modal coupling can also be partially undone after the wavefront correction. However, an AO system will inevitably increase the hardware complexity, and cannot fully compensate for the effects of turbulence, leading to residual inter-mode crosstalk [20], [21]. On the other hand, digital signal processing (DSP) is another powerful approach to mitigate turbulence effects [18], which can reduce the complexity in the optical domain. There have been many reported demonstrations using multiple-input multiple-output (MIMO) DSP to cancel the inter-mode crosstalk in an MDM-FSO system [22], [23]. However, most of them are based on a one-stage MIMO equalizer, which will induce severe noise amplification when the channel matrix is non-unitary (ill-conditioning) [24] due to the joint effect of inter-mode crosstalk and mode-dependent loss after FSO transmission. Moreover, few of them have implemented the transmit-side DSP to mitigate the effects of atmospheric turbulence.

In this work, we combine the adaptive bit loading configuration from our recent European Conference on Optical Communication (ECOC) paper [25] with successive interference cancellation (SIC) DSP at the receiver [26] to demonstrate a high-capacity adaptive transceiver that can combat atmospheric turbulence and realize high-capacity MDM-FSO transmission. In this paper, we dynamically estimate the achievable signal-to-noise ratio (SNR) after linear equalization, and use the estimated SNR to optimize the allocation of modulation formats as well as power to different transmit modes at the transmitter side, and dynamically estimate the channel state information (CSI) and use the estimated CSI to select the detection algorithm with the lowest power consumption which would meet the forward error correction (FEC) requirement. For experimental demonstration, a time-division multiplexed (TDM) frame structure that was

introduced in our previous work [25], [27] is discussed in detail. We employ a spatial light modulator (SLM) to emulate a turbulent multi-modal FSO link. Meanwhile, a commercial transponder and a pair of commercial mode-selective photonic lanterns (MSPLs) for multiplexing and demultiplexing are employed to demonstrate practical applicability. In this work, we experimentally demonstrate an aggregate data rate of 590 Gbit/s in strong turbulence showing the potential of the proposed adaptive transceiver for combating the effects of atmospheric turbulence in MDM-FSO communication systems.

The remainder of this paper is organized as follows: Section II describes an FSO-MIMO system model in atmospheric turbulence and introduces the designed adaptive transceiver for it. Section III shows our proof-of-concept experiment for the emulation of a turbulent MDM-FSO link. Section IV shows our experimental results and performance analysis. Finally, Section V concludes the paper.

Notations: Unless otherwise specified, vectors are denoted by boldface small letters, e.g., \mathbf{x} , while matrices are expressed by capital letters, e.g., \mathbf{X} . $\|\mathbf{x}\|$ denotes the Euclidean norm of \mathbf{x} .

II. PROPOSED ADAPTIVE TRANSCEIVERS

Fig. 1 illustrates the schematic diagram of the proposed adaptive MIMO transceiver working in atmospheric turbulence. Consider an FSO MIMO system comprising N_t transmitters and N_r receivers in atmospheric turbulence [28], [29]. At the receiver side, the channel transfer function matrix can be dynamically estimated. Since an FSO MIMO transfer function matrix is nonunitary, the MIMO receiver is divided into three different parts, i.e., channel estimation, MIMO equalization [30], and MIMO detection. The dynamically estimated SNR after MIMO equalization is sent back to the transmitter to inform bit and power loading at the transmitter with a constant bit rate objective.

A. System Model

Let x_m be the transmitted signal in the m -th time interval, then the received signal is

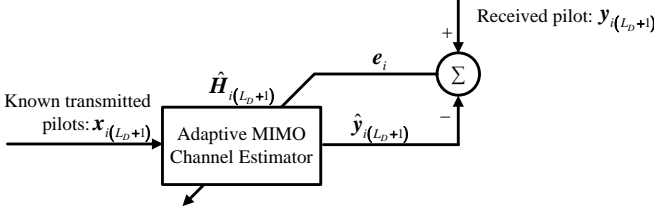


Fig. 2. Illustration of the adaptive MIMO channel estimator working in a time-variant MIMO system.

$$y_m = \sum_{l_M=-L_M/2}^{L_M/2} \mathbf{G}_{m,l_M}^{(r)} \mathbf{H}_{m-l_M} \mathbf{G}_{m,l_M}^{(t)} x_{m-l_M} + n_m, \quad (1)$$

where \mathbf{H} represents the time-variant channel matrix reflecting quasi-static inter-mode crosstalk, diffraction, and atmospheric turbulence, \mathbf{n} the channelized noise, L_M+1 the memory length of the channel, and $\mathbf{G}^{(t)}$ and $\mathbf{G}^{(r)}$ denote the effect of inter-symbol interference (ISI) at the transmitter side and the receiver side, respectively.

As shown in Fig. 1, \mathbf{X} represents a frame of data symbols x_m comprising a number of cells themselves comprising one pilot symbol and L_D data symbols with at least one cell per transmit mode. The pilot symbols are located in the $i(L_D+1)^{\text{th}}$ time intervals where, where i is the cell index $(0, 1, \dots)$.

B. Dynamic Channel Estimation

As shown in Fig. 1, the adaptive signal processing at both transmitter and receiver is based on a dynamically estimated MIMO channel. Following frame synchronization, we compare the product of the known transmitted pilots with the estimated channel transfer function matrix to the received pilots and use the complex least-mean-square (LMS) algorithm with a step size μ to optimize the trade-off between stability and tracking speed [31] and thus to track both amplitude and phase changes of \mathbf{H} due to time-variant atmospheric turbulence, as illustrated in Fig. 2. The estimated channel matrix $\hat{\mathbf{H}}_m$ between two adjacent pilots is set using a conventional linear interpolation algorithm [32].

C. Adaptive MIMO Equalizer

For a unitary system where one has an impulse response mixed with a channel matrix (e.g., few-mode fiber [30]), it is necessary to compensate for both the impulse response and the exchange of power between modes. Conventionally, such a MIMO equalizer [30] would be optimized towards an objective function of the transmitted pilot sequence. However, for a non-unitary channel, the power loss (or mode-dependent loss) can lead to noise amplification, degrading the performance [24]. Here we adopt a two-stage process, where the first stage targets the impulse response, and the second stage the mode mixing. In the first stage (MIMO equalizer) we adopt a similar structure to the conventional MIMO equalizer, but with a modified objective function of the (impulse response free) channel matrix acting on the known pilot/training sequence. This objective function clearly does not equalize the mode mixing, but instead compensates for the impact of the channel memory

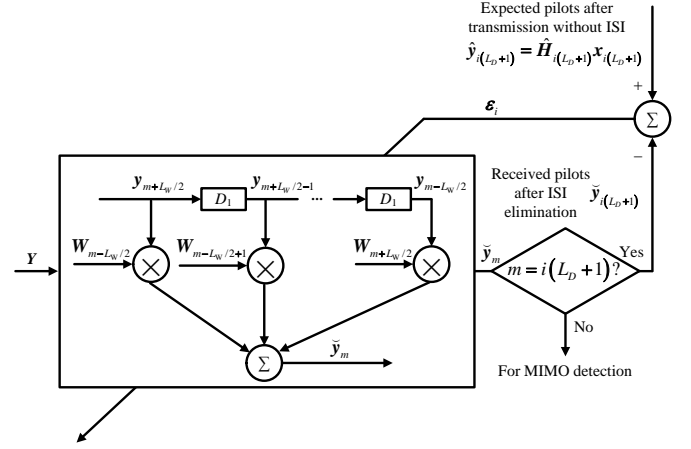


Fig. 3. The structure of the adaptive MIMO equalizer, where D_1 denotes delay of one symbol period.

(transmitter effects times the channel matrix plus receiver effects). This stage is then followed by an independent memoryless MIMO decoder that can suppress such noise amplification by leveraging an advanced detection algorithm.

Fig. 3 depicts the structure of the adaptive MIMO equalizer used in the proposed transceiver, where the equalized signal is a weighted sum of L_W+1 successive received symbols, as

$$\tilde{y}_m = \sum_{l_W=-L_W/2}^{L_W/2} \mathbf{W}_{m+l_W} y_{m-l_W}, \quad (2)$$

where y_{m-l_W} is the received signal in the $(m - l_W)$ -th time interval, and \mathbf{W}_{m+l_W} is the corresponding equalizer coefficient matrix. As shown in Fig. 3, the equalizer taps are updated according to the difference between the equalized signal and the expected pilots multiplied by the estimated channel matrix (Section II.B).

D. Adaptive MIMO Detection

After compensation of the transmitter and receiver impulse responses (Section II.C), the transmitted signal can be estimated using a MIMO decoder. We consider three conventional decoder algorithms and propose a novel adaptive algorithm to dynamically select the most appropriate algorithm for each frame.

1. *Minimum mean-squared error (MMSE)*: MMSE is a linear detection algorithm that minimizes the mean-squared error [33] by using the estimated channel matrix and noise variance. It has the lowest complexity among the algorithms considered. Although with an additional regularization term, MMSE is more robust against the aforementioned noise amplification than the simplest zero-forcing detector, it is still vulnerable to a nonunitary channel compared to the other MIMO detection algorithms considered in this work.

2. *Successive interference cancellation (SIC)*: SIC is one of the most popular detection algorithms for MIMO systems. The main idea of SIC is successively canceling out the interference of the best channel from the remaining channels using decoded

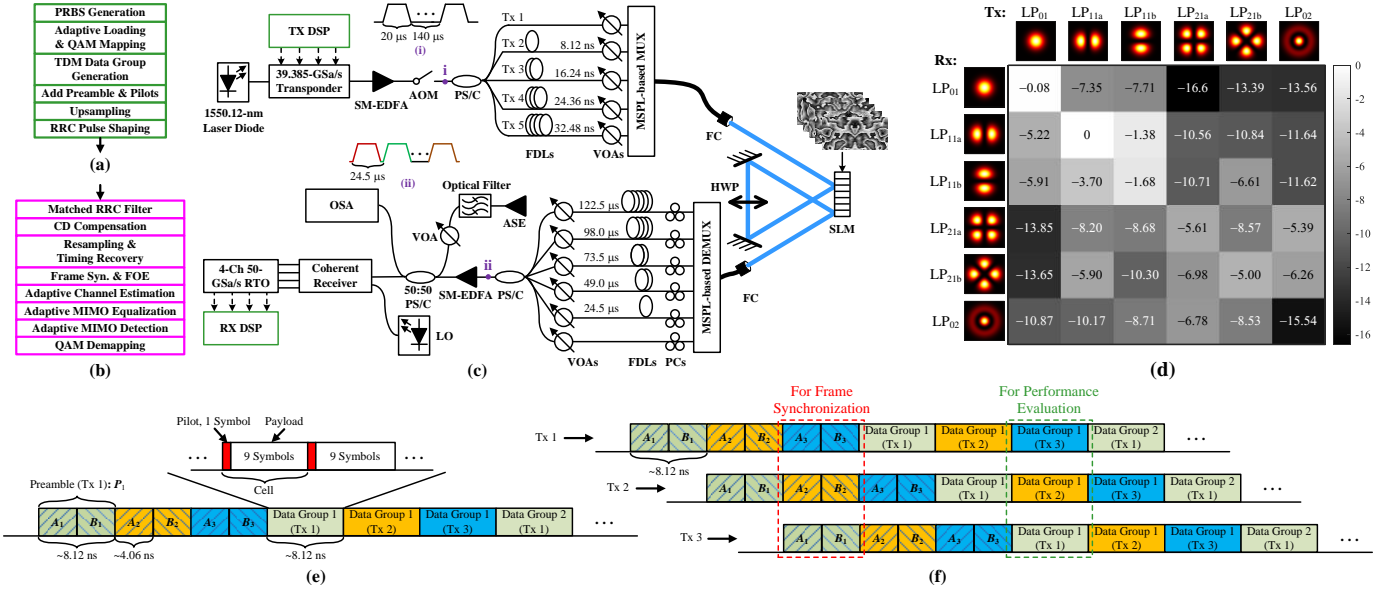


Fig. 4. Proof-of-concept experiment for verifying the proposed adaptive transceiver in turbulent MDM-FSO systems: DSP at (a) the transmitter side, and (b) the receiver side, respectively. (c) Experimental setup (AOM, acousto-optic modulator; ASE, amplified spontaneous emission; EDFA, erbium-doped fiber amplifier; FC, fiber collimator; FDL, fiber delay line; HWP, half-wave plate; LO, local oscillator; RTO, real-time oscilloscope; OSA, optical spectrum analyzer; PC, polarization controller; PS/C, power splitter/coupler; SLM, spatial light modulator; VOA, variable optical attenuator); Inset: (i) signal bursts after AOM; (ii) TDM signal bursts after interleaving. (d) Measured crosstalk matrix (dB) of MSPL, normalized to LP_{11a}. Example (e) TDM frames generated at the transmitter side and (f) synchronized streams after power splitter and FDLs (3 transmitters for illustration).

bits and the estimated channel matrix, leading to better performance than MMSE with a moderate increase in complexity [34].

3. *Maximum likelihood detection (MLD)*: MLD is the optimal MIMO detection algorithm [35], which operates by minimizing the probability of error over all possible transmitted vectors. It has an extremely high computational complexity that is exponential in N_t and the order of the modulation format.

4. *Combined SIC-MLD*: One drawback of SIC is that detection errors on one channel are locked in and impact the remaining channels giving the potential for error propagation. This particularly impacts the last channel considered and deep fades. To mitigate this, we also consider combining SIC and MLD, aiming to only apply MLD to the signal vectors that are more likely to be degraded by error propagation after SIC. The metric is based on the decision-directed error vector magnitude (EVM) for the symbol, as

$$d_{E,m} = \frac{\|\hat{\mathbf{x}}_{\text{SIC},m} - \tilde{\mathbf{x}}_{\text{SIC},m}\|}{D_R}, \quad (3)$$

where $\hat{\mathbf{x}}_{\text{SIC},m}$ is the recovered signal vector after SIC, $\tilde{\mathbf{x}}_{\text{SIC},m}$ is the signal vector after decision, and D_R denotes the normalization reference. The normalization reference is scaled to the minimum Euclidean distance of all the modulation formats used in a frame. Symbols corresponding to the largest 10% of EVMs are passed to MLD. As the complexity of SIC is typically much lower than MLD, this work reduces the overall complexity by almost an order of magnitude.

E. Adaptive Bit and Power Loading

Due to the different conditions experienced by the signals

from different transmitters, they will have different SNRs after transmission. To maximize the throughput of the system, we employ adaptive bit and power loading at the transmitter [36], as shown in Fig. 1. Here, we adopt Chow's algorithm [37], where the bit allocation is applied first. For a fixed data rate and total launch power objective, more bits are allocated to transmitters with higher SNR, and vice versa. The power distribution was adjusted by controlling the peak-to-peak drive amplitude and typically resulted in an approximately 3-dB SNR difference between two adjacent modulation formats.

The CSI applied to the transmitted payload of one frame is determined from an earlier frame, as determined by processing delays and the channel round trip time. If the channel fluctuations are more rapid than this timescale, inaccuracy of the estimated CSI can result in degradation of the adaptive loading scheme. In a ground-to-ground FSO communication system, if we consider a typical wavelength of 1550 nm, strong turbulence (a refractive-index structure constant of $1.7 \times 10^{-14} \text{ m}^{-2/3}$), and a wind velocity of 21 m/s, and compare the Greenwood time constant [38], [39] to the round trip time of the link, it is easy to show that the maximum link length is ~ 10 km for ground-to-ground FSO communications in turbulence.

For a low earth orbit satellite-to-ground FSO system, even with a 0-degree zenith angle, the corresponding Greenwood time constant is ~ 4 ms [40] leading to a maximum link length of ~ 60 km, precluding the use of receiver-directed adaptive loading in FSO MIMO satellite applications.

III. PROOF-OF-CONCEPT EXPERIMENT

A. Experimental Setup and DSP

The proof-of-concept experiment including experimental setup and offline DSP is depicted in Fig. 4. In this work, we

adopted 5 transmit modes and 6 receive modes for robust transmission, which outperforms 5 receive modes [26], [27]. Two schemes that have different symbol rates but similar data rates have been considered in this work: (1) 19.7 Gbaud, 30 bits allocated to 10 channels (5 transmit modes \times 2 polarizations); (2) 29.5 Gbaud, 20 bits allocated to 10 channels.

As shown in Fig. 4(a), at the transmitter side, a pseudorandom binary sequence (PRBS, $2^{15}-1$ bits) was first generated for quadrature amplitude modulation (QAM) mapping, where the order of modulation formats (number of bits) and the power were adaptively allocated (Section II.E). The payload symbols were then assembled into frames with preambles and 4-QAM pilot symbols. To emulate fully independent transmitters enabling channelized precoding schemes, we used a TDM frame structure as shown in Fig. 4(e), where only 3 transmitters were shown for illustration. Each frame written to the transponder comprised a symmetric training sequence of 8.12 ns for each transmitter mode to enable frame synchronization and frequency offset estimation (FOE) [27], followed by a repeating structure of forty-nine 8.12-ns data groups with data rotating through the channels (2% framing overhead). Each data group consisted of 16 cells at 19.7 Gbaud, or 24 cells at 29.5 Gbaud, and each cell had one pilot symbol and 9 payload symbols (10% pilot overhead). The generated frames were then up-sampled to 39.385 GSa/s (limited by the onboard arbitrary waveform generator) with root-raised cosine (RRC) pulse shaping (0.05 roll-off factor), after which the generated TDM signal was sent to a commercial transponder (Ciena Wavelogic 3) for the generation of a dual-polarization QAM (DP-QAM) optical signal at 1550.12 nm. After amplification by a single-mode (SM) erbium-doped fiber amplifier (EDFA), the optical signal was gated by an acousto-optic modulator (AOM). The gate width was 20 μ s and passed a block of more than 2,413 data groups corresponding to over 2^{18} payload symbols at 19.7 Gbaud. The gating period was set to 160 μ s to allow room for a block per mode at the receiver, as illustrated in Inset (i) of Fig. 4(c). After passing through a power splitter and an array of variable fiber delay lines (FDLs), the preambles and data groups were time aligned with a precision of 2% of a sample period, but delayed by $(n_i - 1) \times 8.12$ ns. Therefore, as shown in Fig. 4(f), the preambles and data groups representing different transmitters were aligned for frame synchronization where all training symbols are aligned (highlighted in red) or performance evaluation where all transmitter payloads are aligned in the correct order (highlighted in green) at the receiver side. It should be noted that for a 5-channel system, one-fifth of the groups comprised the originally intended data patterns. 5 variable optical attenuators (VOA) were employed to balance any transmitter-side mode-dependent loss (MDL), after which a commercial MSPL (Phoenix Photonics, Ltd.) was used for MDM implementation. The multiplexed optical signal had a burst power of about 8.7 dBm, and the average burst power per transmit mode was about 1.7 dBm. MDM optical signal was then launched into free space through a fiber collimator (FC) with a focal length of 18.4 mm and a lens diameter of $D = 8.4$ mm. The signal was then reflected from an SLM, polarization

rotated with a half-wave plate, and reflected again from a different portion of the SLM to emulate atmospheric turbulence for both polarization components of the optical signals. Some example patterns displayed on the SLM are presented as the insets in Fig. 4(c).

At the receiver side, another FC was used to couple the light into the few-mode fiber, where the coupling loss was approximately 6.2 dB. The MDM signal was then demultiplexed by another MSPL. The measured normalized crosstalk matrix of the pair of MSPLs (without VOA balancing) is shown in Fig. 4(d). As we can see from the figure, the linearly polarized (LP) modes were excited with relatively large inter-mode crosstalk. The resultant 6 streams, one per mode, were delayed by another array of FDLs with an incremental delay of 24.5 μ s and then combined to produce a TDM stream of successive 20- μ s bursts of frames corresponding to the detected signal from each mode. These were optically amplified, noise loaded, and detected by a single coherent receiver where the 24.5- μ s delays were digitally reversed, this whole process emulating 6 independent receivers. Before combination of the streams, an array of polarization controllers (PCs) was employed along with another array of VOAs to minimize the impact of quantization noise from analog-to-digital conversion. The interleaved signal is illustrated in Inset (ii) of Fig. 4(c). The optical signal-to-noise ratio (OSNR) of the interleaved signal was measured by an optical spectrum analyzer (OSA) and represents an average OSNR over all modes. At the coherent receiver, the signal burst power was ~ 8.25 dBm, and the free-running local oscillator (LO) has a power of ~ 12 dBm. The resultant electrical signal was captured by a 50-GSa/s four-channel real-time oscilloscope with an analog bandwidth of 23 GHz and a typical effective number of bits of 5.4 bits.

The receiver-side DSP is shown in Fig. 4(b). After performing matched RRC filtering, fixed chromatic dispersion (CD) compensation for the receiver delay lines, resampling, and timing recovery, the frame synchronization and the FOE were blindly realized by using the preambles [27]. The channel state including inter-mode crosstalk and carrier phase was then dynamically estimated by the adaptive channel estimator, after which the adaptive MIMO equalization leveraging the estimated channel transfer function matrix was applied to the signal before performing MIMO detection. By employing the four MIMO detection algorithms given in Section II.D, the signal performance after QAM demapping was finally evaluated to compare their suitability under different channel conditions.

B. Emulation of Turbulence

For long-distance free-space links, we need to consider both tip-tilt aberrations and high-order aberrations in MDM systems [41]-[44]. In general, we can use the ensemble average known as the phase structure function to describe the aberrations introduced by atmospheric turbulence [45].

In this work, a single-phase screen was displayed on an SLM to emulate thin air turbulence [46]. The screens used were generated by implementing a power spectrum inversion method,

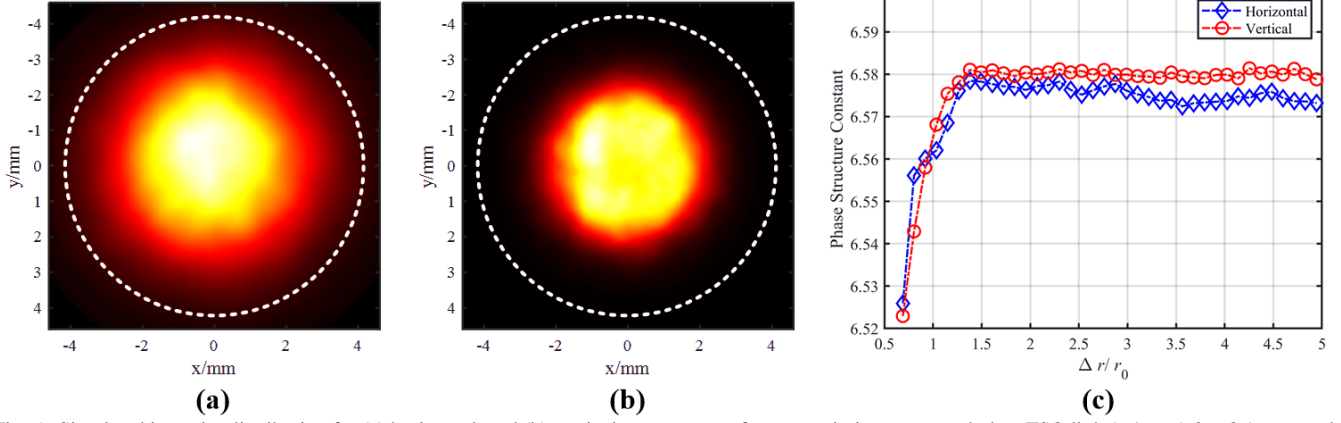


Fig. 5. Simulated intensity distribution for (a) horizontal, and (b) vertical components after transmission over a turbulent FSO link ($D/r_0 = 5$, $l_0 = 0.1$ mm, and $L_0 = 10$ m), where the beam size of the two components was slightly different because we needed to pass the light through the SLM twice to apply the turbulence to both polarization components. (c) Simulated phase structure constant as a function of $\Delta r/r_0$ for horizontal (blue diamonds) and vertical (red circles) components.

based on the von Kármán spectrum [48] with Fourier series coefficients, $c_{a,b}$, in the form,

$$c_{a,b} = w_{a,b} \frac{\sqrt{0.023}}{L} \left(\frac{2}{r_0} \right)^{\frac{5}{6}} \left(\frac{a^2 + b^2}{L^2} + \frac{1}{L_0^2} \right)^{-\frac{11}{12}} \sqrt{e^{-\left(\frac{a^2 + b^2}{L^2} \right) \left(\frac{2\pi l_0}{5.92} \right)^2}}, \quad (4)$$

where $w_{a,b}$ is a random array obeying complex circular Gaussian statistics with zero-mean and unit-variance. L is the length of the pattern (8.832 mm in this work). The power spectrum is also determined by the largest (L_0) and smallest (l_0) eddy sizes of a turbulent channel. r_0 is the Fried parameter, which is a measure of the transverse distance scale over which the refractive index is correlated [47].

To accurately represent modes such as tilt aberration, the sub-harmonic method proposed by Lane *et al* [44], [49] was employed. A specific phase screen $\phi_{x,y}$ can then be computed as a sum of $N_p + 1$ independent screens using the formula,

$$\phi_{x,y} = \sum_{a=-\infty}^{+\infty} \sum_{b=-\infty}^{+\infty} c_{a,b} e^{j2\pi \left(\frac{ax+by}{L} \right)} + \sum_{p=1}^{N_p} \sum_{a=-1}^1 \sum_{b=-1}^1 c_{a,b,p} e^{j2\pi \left(\frac{ax+by}{L} \right)}, \quad (5)$$

Herein, spatial frequencies of low-frequency components distribute on a 3×3 grid of 2D space, where the frequency grid spacing for each value of p is $1/(3^p L)$, corresponding to a Fourier series coefficient of $c_{a,b,p}$.

We have made a propagation simulation from the transmitter to the receiver based on the real parameters in the experiment, where we set $D/r_0 = 5$ for Gaussian modes, $l_0 = 0.1$ mm, and $L_0 = 10$ m. In our experiment, we used r_0 to determine the turbulence strength. The intensity distribution for horizontal and vertical components is shown in Fig. 5(a) and (b), where the white dashed circle represents the diameter of the receiver. We can see from the figure that since we needed to pass the

light through the SLM twice to apply the turbulence to both polarization components, the beam size of the received two polarization components was slightly different but all can be captured by our FC. In this work, misalignment and beam expansion were not considered. The phase structure function [45] for horizontal and vertical polarization components was calculated to evaluate the phase fluctuation created by the turbulence phase screen. In Fig. 5(c), we present the phase structure function of horizontal and vertical components at different $\Delta r = \|\mathbf{r}_1 - \mathbf{r}_2\|$. We can see from the figure that the horizontal and vertical polarizations were distorted in approximately the same way in our channel setup.

IV. EXPERIMENTAL RESULTS

In our experiment, we changed the turbulence strength by setting different values of r_0 , i.e., 0.5 mm, 0.9 mm, and 1.1 mm. A smaller r_0 value leads to a stronger turbulence effect. To verify the performance of individual aspects of our DSP, single, but typical, turbulence patterns were employed in Section IV. A – C, while to verify robustness against turbulence for the whole system, 12 independent turbulence patterns were employed in Section IV. D.

A. Adaptive Channel Estimation

We first investigated the convergence performance of the adaptive channel estimator as shown in Fig. 6, where the symbol rate was set to 19.7 GBd, and 30 bits were allocated across all 10 channels (5 modes \times 2 polarizations) without adaptive loading (uniform 8-QAM), corresponding to a line rate of 591 Gbit/s. MMSE detection was used at the receiver.

Fig. 6(a) presents example changes of tracking errors over time for different step sizes of the LMS-based adaptive channel estimator. When the step size is too small, the adaptive channel estimator fails to converge (red), while if too large it becomes influenced by noise (black). In Fig. 6(b), the impact of step size on the EVM performance of all 10 channels is shown. We can see from the figure that all channels have almost the same optimal step size, indicating the importance of its optimization.

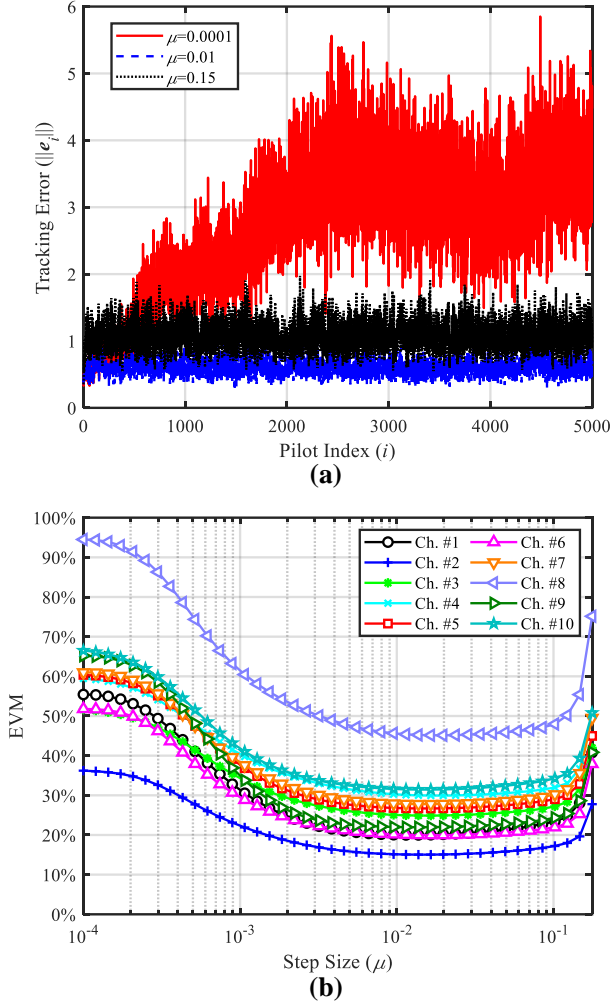


Fig. 6. (a) Example changes of tracking errors over time for a step size of 0.0001 (red solid line), 0.01 (blue dashed line), 0.15 (black dotted line), respectively, in the adaptive channel estimator. (b) EVM performance of all 10 channels versus step size (OSNR = 29.25 dB, $r_0 = 0.9$ mm, MMSE decoder).

B. Adaptive Loading

Next, we verified the impact of adaptive loading on atmospheric turbulence resiliency. Fig. 7 shows the transmission performance of the signals with and without adaptive loading for different levels of turbulence, where the symbol rate and the total number of bits were 19.7 GBd and 30 bits, respectively, and MMSE MIMO detection was employed at the receiver. We can see from the figure that adaptive loading can bring on OSNR sensitivity improvement with and without turbulence. For weaker turbulence ($r_0 = 1.1$ mm), the adaptive loading gain increases from ~ 2.3 dB without turbulence to ~ 5.2 dB with turbulence. For stronger turbulence ($r_0 = 0.9$ mm), adaptive loading is required to reach the hard-decision forward error correction (HD-FEC) threshold of 4.7×10^{-3} [50].

The performance improvement from adaptive loading can be explained with reference to Fig. 8, where we present the constellation diagrams of all channels of the MDM signals with and without adaptive loading. With a uniform modulation format (8-QAM) and power applied, there was a large variation in BER and SNR, with two channels with BERs beyond the

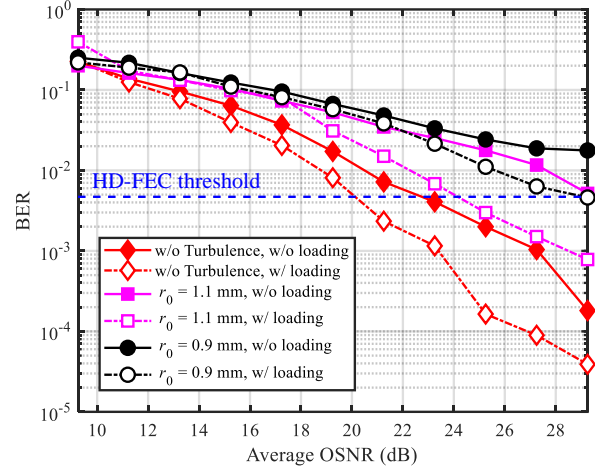


Fig. 7. Transmission performance of the signals with (dashed line, open symbols) and without (solid line, filled symbols) adaptive loading, for turbulence free (red diamonds) and with turbulence scaled with r_0 of 1.1 mm (magenta squares) and 0.9 mm (black circles) (19.7 GBd, 30 bits allocated, $D = 8.4$ mm, $l_0 = 1$ mm, $L_0 = 10$ m, MMSE decoder).

HD-FEC threshold (highlighted in red), leading to an average BER of 5.2×10^{-3} . On the other hand, as shown in Fig. 8(b), when the optimal modulation formats and power were allocated, the BERs became more uniform and all of them were below the HD-FEC threshold, leading to an average BER of 7.8×10^{-4} . It should be noted that the residual variation in BER observed in Fig. 8(b) can be attributed to a small penalty in the allocation algorithm.

C. MIMO Detection

We then evaluated the performance of the proposed receiver-side DSP against atmospheric turbulence without adaptive loading. Considering the high computational complexity of MLD, we only allocated 20 bits across all 10 channels without adaptive loading (uniform 4-QAM), while increasing the symbol rate to 29.5 GBd in this subsection, also leading to a line rate of 590 Gbit/s.

Fig. 9 shows the transmission performance of the signals with different MIMO decoders. We can see from the figure that the conventional MMSE decoder (circles) shows the worst performance in all cases, which we attribute to noise amplification. When SIC (squares) is used, this effect can be mitigated, reducing the average OSNR required. Meanwhile, by applying additional MLD to 10% of the signal vectors that have the largest decision-directed EVM (diamonds), the proposed combined SIC-MLD scheme further improves the transmission performance, reducing the turbulence penalty to less than 3 dB. We also observe that the performance difference between MIMO decoders increases with increasing turbulence.

D. Combined Adaptive Transceiver

In order to verify the performance of the whole system, the total number of bits allocated to the 10 channels was set to 20, and the signal symbol rate was 29.5 GBd, leading to a line rate of 590 Gbit/s. The average OSNR of the signal without turbulence was initially set to ~ 30 dB before applying turbulence by the SLM for 12 turbulence realizations with an r_0

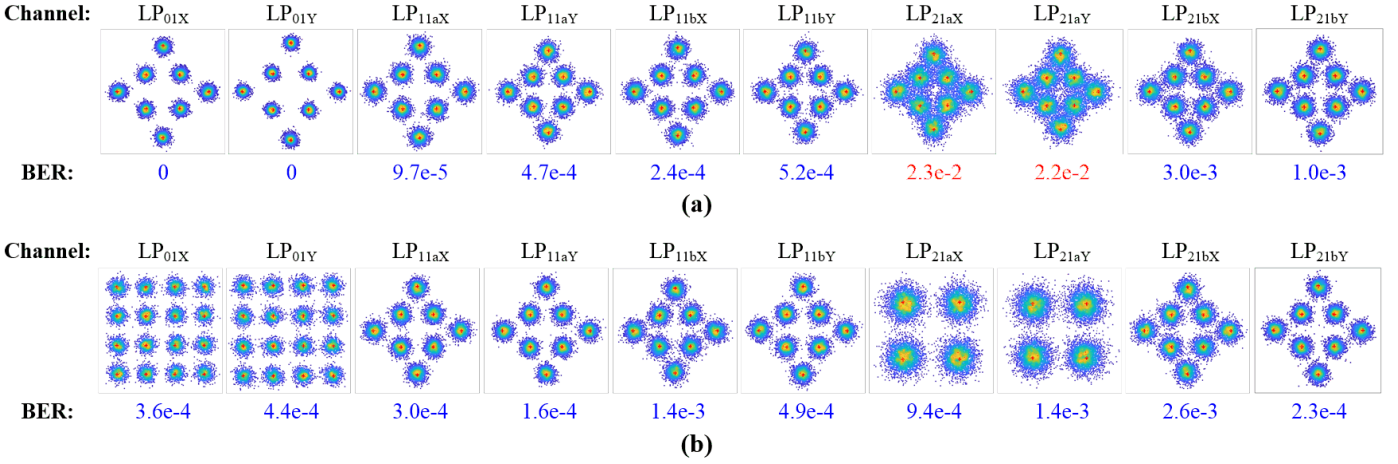


Fig. 8. Constellation diagrams of all channels of the MDM signals (a) without and (b) with adaptive loading after transmission over a turbulent FSO link (OSNR = 29.25 dB, $r_0 = 1.1$ mm, MMSE decoder). The BER below the HD-FEC threshold of 4.7×10^{-3} is highlighted in blue, while the BER above the HD-FEC threshold is highlighted in red.

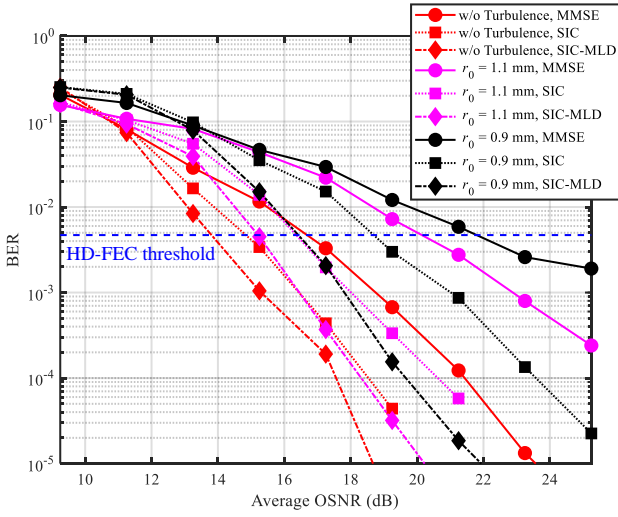


Fig. 9. Transmission performance of the signals for turbulence free (red) and with turbulence scaled with r_0 of 1.1 mm (magenta) and 0.9 mm (black), and demodulated with MMSE (circles, solid line), SIC (squares, dotted line) and SIC-MLD (diamonds, dash-dotted line) MIMO decoders (29.5 Gbd, 20 bits allocated, without adaptive loading).

value of 0.5 mm (strong turbulence). Fig. 10(a) shows the BER performance of the signals as different elements of the proposed signal processing were added for these 12 turbulence realizations. The corresponding plot box is also presented in Fig. 10(b) to show the statistic of the BER performance for different DSP schemes. The results show that combining adaptive loading (2-, 4-, and 8-QAM) and more powerful MIMO decoders can bring on the reduction of BER not only compared to the conventional scheme without adaptive loading and with simple MMSE detection, but also the scheme only with adaptive loading or only with powerful MIMO decoders. The combined SIC-MLD has a similar curve and only shows a marginal degradation compared to MLD-only, indicating its similar performance but much lower computational complexity.

The results show that the proposed adaptive transceiver can perform various signal processing schemes with different abilities against turbulence, leading to higher flexibility compared to the conventional one-stage MIMO equalizer.

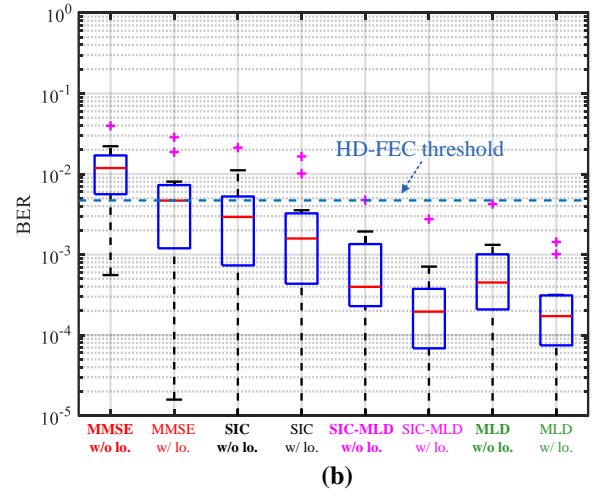
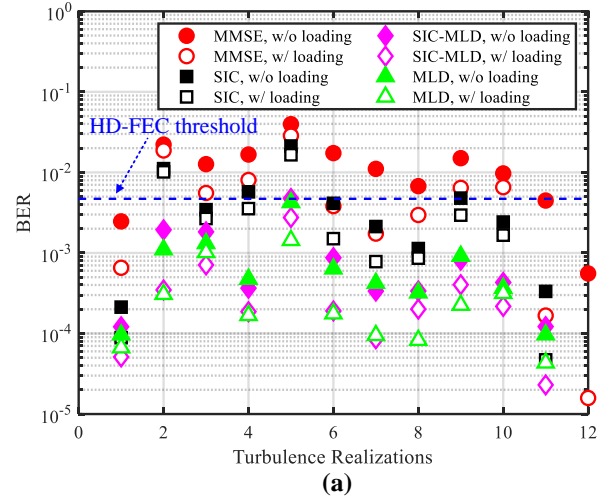


Fig. 10. (a) BERs of the signals (29.5 Gbd, 20 bits allocated) with (open symbols) and without (filled symbols) adaptive loading, and demodulated with MMSE (red circles), SIC (black squares), SIC-MLD (magenta diamonds) and MLD-only (green triangles) MIMO decoders under 12 turbulence realizations ($r_0 = 0.5$ mm), and (b) the corresponding box plot for different schemes.

Meanwhile, different from AO systems, the proposed scheme does not increase hardware complexity in the optical domain. In practical applications, the proposed adaptive transceiver is

able to dynamically switch between schemes based on the latest estimated channel conditions (e.g., OSNR and the condition number of the channel matrix), and pick the most suitable scheme meeting the FEC threshold requirement but at the minimum complexity. Nevertheless, more data and tests under different scenarios are required to further verify the proposed adaptive transceiver, which will be studied in our future work.

V. CONCLUSION

In this paper, we have designed an adaptive transceiver for improving the atmospheric turbulence resiliency of an MDM-FSO communication system. Compared to the scheme based on AO, the proposed adaptive transceiver does not increase the hardware complexity in the optical domain. Meanwhile, by dividing the conventional one-stage MIMO equalizer into three stages, in the proposed scheme, it becomes possible to utilize advanced MIMO decoders to further improve transmission performance and combat turbulence effects. The adaptive loading scheme also provides a potential solution to maximize the throughput of the system at the transmitter side. Therefore, by allocating optimal modulation formats and power to different channels at the transmitter side and employing the most suitable MIMO decoder at the receiver side, the communication system is able to achieve an average BER below the target FEC threshold while maintaining the system power consumption as low as possible. In our experimental demonstration, we employed an SLM to emulate atmospheric turbulence, and we have successfully demonstrated 590-Gbit/s MDM-FSO transmission with 5 transmit modes and 2 polarizations, under 12 random strong turbulence realizations. All results indicate the great potential of the proposed high-capacity adaptive transceiver to combat the atmospheric turbulence present in an outdoor MDM-FSO communication system.

ACKNOWLEDGMENT

We would like to thank Ciena and Dr. Charles Laperle for kindly providing the WaveLogic 3 transponder used in our experiments. We also thank Dr. Vitor Ribeiro for fruitful discussions.

REFERENCES

- [1] F. Tonini et al., "Cost-optimal deployment of a C-RAN with hybrid fiber/FSO fronthaul," *IEEE/OSA J. Opt. Commun. Netw.*, vol. 11, no. 7, pp. 397–408, 2019.
- [2] M. P. J. Lavery et al., "Tackling Africa's digital divide," *Nature Photon.*, vol. 12, pp. 249–252, May 2018.
- [3] Z. Ghassemlooy et al., "Emerging optical wireless communications—advances and challenges," *IEEE J. Sel. Areas Commun.*, vol. 33, no. 9, pp. 1738–1749, Sep. 2015.
- [4] F. P. Guiomar et al., "Coherent Free-Space Optical Communications: Opportunities and Challenges," *J. Lightwave Technol.*, vol. 40, no. 10, pp. 3173–3186, 2022.
- [5] M. A. Khalighi and M. Uysal, "Survey on free space optical communication: A communication theory perspective," *IEEE Commun. Surveys Tuts.*, vol. 16, no. 4, pp. 2231–2258, 4th Quart., 2014.
- [6] B. I. Bitachon et al., "Tbit/s Single Channel 53 km Free-Space Optical Transmission -Assessing the Feasibility of Optical GEO-Satellite Feeder Links," in *Proc. ECOC*, Basel, Switzerland, 18–22 Sep. 2022, Paper Th3A.6.
- [7] A. Trichili, M. A. Cox, B. S. Ooi, and M.-S. Alouini, "Roadmap to free space optics," *J. Opt. Soc. Amer. B*, vol. 37, no. 11, pp. 184–201, Nov. 2020.
- [8] P. J. Winzer, D. T. Neilson, and A. R. Chraplyvy, "Fiber optic transmission and networking: The previous 20 and the next 20 years," *Opt. Express*, vol. 26, no. 18, pp. 24190–24239, 2018.
- [9] J. Wang et al., "Terabit free-space data transmission employing orbital angular momentum multiplexing," *Nat. Photon.*, vol. 6, no. 7, pp. 488–496, 2012.
- [10] M. J. Padgett, "Orbital angular momentum 25 years on [invited]," *Opt. Exp.*, vol. 25, no. 10, pp. 11265–11274, 2017.
- [11] A. Trichili et al., "Communicating using spatial mode multiplexing: Potentials, challenges and perspectives," *IEEE Commun. Surv. Tut.*, vol. 21, no. 4, pp. 3175–3203, Oct.–Dec. 2019.
- [12] A. E. Willner et al., "Recent advances in high-capacity free-space optical and radio-frequency communications using orbital angular momentum multiplexing," *Philosoph. Trans. Roy. Soc. London A: Math., Phys. Eng. Sci.*, vol. 375, no. 2087, 2017.
- [13] N. Zhao, X. Li, G. Li, and J. M. Kahn, "Capacity limits of spatially multiplexed free-space communication," *Nat. Photon.*, Vol. 9, no. 12, pp. 822–826, 2015.
- [14] K. Pang et al., "400-gbit/s qpsk free-space optical communication link based on four-fold multiplexing of hermite-gaussian or laguerre-gaussian modes by varying both modal indices," *Opt. Lett.*, Vol. 43, no. 16, pp. 3889–3892, 2018.
- [15] M. A. Cox et al., "The resiliency of Hermite-and Laguerre- Gaussian modes in turbulence," *J. Lightwave Technol.*, vol. 37, no. 16, pp. 3911–3917, 2019.
- [16] J. A. Anguita et al., "Turbulence-induced channel crosstalk in an orbital angular momentum-multiplexed freespace optical link," *Appl. Opt.*, vol. 47, no. 13, pp. 2414–2429, May 2008.
- [17] N. Chandrasekaran and J. H. Shapiro, "Turbulence-induced crosstalk in multiple-spatial-mode optical communication," in *Proc. CLEO*, San Jose, CA, May 6–11, 2012, Paper CF31.6.
- [18] A. E. Willner et al., "Perspectives on Advances in High-Capacity, Free-Space Communications Using Multiplexing of Orbital-Angular-Momentum Beams," *APL Photonics*, vol. 6, no. 3, 2021, p. 030901.
- [19] Y. Kaymak et al., "A survey on acquisition, tracking, and pointing mechanisms for mobile free-space optical communications," *IEEE Commun. Surveys Tuts.*, vol. 20, no. 2, pp. 1104–1123, 2nd Quart., 2018.
- [20] Y. Ren et al., "Adaptive-optics-based simultaneous pre-and post-turbulence compensation of multiple orbital-angular-momentum beams in a bidirectional free-space optical link," *Optica*, vol. 1, no. 6, pp. 376–382, 2014.
- [21] X. Su et al., "Experimental Demonstration of Adaptive-Optics-Based Turbulence Mitigation in a Mode-Multiplexed Free-Space Optical Link by Using both Radial and Azimuthal Spatial Indices," in *Proc. OFC*, paper M4I.2, 2022.
- [22] H. Huang et al., "Crosstalk mitigation in a free-space orbital angular momentum multiplexed communication link using 4 × 4 MIMO equalization," *Opt. Lett.*, vol. 39, no. 15, pp. 4360–4363, 2014.
- [23] Y. Ren et al., "Atmospheric turbulence mitigation in an OAM-based MIMO free-space optical link using spatial diversity combined with MIMO equalization," *Opt. Lett.*, vol. 41, no. 11, pp. 2406–2409, 2016.
- [24] D. Tse and P. Viswanath, *Fundamentals of Wireless Communication*. Cambridge, U.K.: Cambridge Univ. Press, 2005.
- [25] Z. Hu et al., "Single-Wavelength Terabit Multi-Modal Free Space Optical Transmission with Commercial Transponder," in *Proc. ECOC*, Basel, Switzerland, 18–22 Sep. 2022, Paper Tu4F.5.
- [26] Y. Li et al., "Enhanced Atmospheric Turbulence Resiliency with Successive Interference Cancellation DSP in Mode Division Multiplexing Free-Space Optical Links," *J. Lightw. Technol.*, vol. 40, no. 24, pp. 7769–7778, 2022.
- [27] Z. Hu et al., "Single-wavelength transmission at 1.1-Tbit/s net data rate over a multimodal free-space optical link using commercial devices," *Opt. Lett.*, vol. 47, no. 14, pp. 3495–3498, 2022.
- [28] N. Cvijetic, S. G. Wilson, and M. Brandt-Pearce, "Performance bounds for free-space optical MIMO systems with APD receivers in atmospheric turbulence," *IEEE J. Sel. Areas Commun.*, vol. 26, no. 3, pp. 3–12, Apr. 2008.
- [29] E. Bayaki, R. Schober, and R. Mallik, "Performance analysis of MIMO free-space optical systems in Gamma-Gamma fading," *IEEE Trans. Commun.*, vol. 57, no. 11, pp. 3415–3424, Nov. 2009.

- [30] R. G. H. van Uden et al., "MIMO equalization with adaptive step size for few-mode fiber transmission systems," *Opt. Exp.*, vol. 22, no. 1, pp. 119–126, Jan. 2013.
- [31] B. Widrow, J. Mccool, and M. Ball, "The complex LMS algorithm," *Proc. IEEE*, vol. 55, pp. 719–720, 1974.
- [32] J. Benesty, J. Chen, and Y. Huang, "Time-delay estimation via linear interpolation and cross correlation," *IEEE Trans. Speech Audio Process.*, vol. 12, no. 5, pp. 509–519, Sep. 2004.
- [33] J. G. Proakis and M. Salehi, *Digital Communications*, 5th ed. New York: McGraw-Hill, 2008.
- [34] G. J. Foschini et al., "Simplified processing for high spectral efficiency wireless communication employing multi-element arrays," *IEEE J. Select. Area Commun.*, vol. 17, pp. 1841–1852, Nov. 1999.
- [35] D. C. Chang and D. L. Guo, "Spatial-division multiplexing mimo detection based on a modified layered osic scheme," *IEEE Trans. Wireless Commun.*, vol. 12, no. 9, pp. 4258–4271, Sept. 2013.
- [36] G. Kulkarni, S. Adlakha, and M. Srivastava, "Subcarrier allocation and bit loading algorithms for OFDMA-based wireless networks," *IEEE Trans. Mobile Comput.*, vol. 4, no. 6, pp. 652–662, Nov./Dec. 2005.
- [37] P. S. Chow, J. M. Cioffi, and J. A. C. Bingham, "A practical discrete multitone transceiver loading algorithm for data transmission over spectrally shaped channels," *IEEE Trans. Commun.*, vol. 48, pp. 772–775, 1995.
- [38] B. Göhler and P. Lutzmann, "Range accuracy of a gated-viewing system as a function of the number of averaged images," in *ElectroOptical Remote Sensing, Photonic Technologies, and Applications*, vol. 8542, 2012, pp. 37–44.
- [39] D. L. Fried, "Time-delay-induced mean-square error in adaptive optics," *J. Opt. Soc. Am. A*, vol. 7, no. 7, 1224–1225, 1990.
- [40] M. T. Gruneisen et al., "Adaptive spatial filtering of daytime sky noise in a satellite quantum key distribution downlink receiver", *Opt. Eng.*, vol. 55, no. 2, 026104, 2016.
- [41] M. P. J. Lavery et al., "Free-space propagation of high-dimensional structured optical fields in an urban environment," *Science Advances*, vol. 3, no. 10, 2017.
- [42] M. P. J. Lavery, "Vortex instability in turbulent free-space propagation," *New Journal of Physics*, vol. 20, no. 4, p. 043023, 4 2018.
- [43] X. Gu, L. Chen, and M. Krenn, "Phenomenology of complex structured light in turbulent air," *Opt. Express*, vol. 28, no. 8, pp. 11033–11050, 2020.
- [44] M. Chen and M. P. J. Lavery, "Optical angular momentum interaction with turbulent and scattering media," in *Structured Light for Optical Communication*. Elsevier, 2021, pp. 237–258.
- [45] G. A. Tyler and R. W. Boyd, "Influence of atmospheric turbulence on the propagation of quantum states of light carrying orbital angular momentum," *Opt. Lett.*, vol. 34, no. 2, pp. 142–144, 2009.
- [46] B. Rodenburg et al., "Influence of atmospheric turbulence on states of light carrying orbital angular momentum," *Opt. Lett.*, vol. 37, no. 17, pp. 3736–3737, 5 2012.
- [47] D. L. Fried, "Statistics of a Geometric Representation of Wavefront Distortion," *JOSA*, vol. 55, no. 11, pp. 1427–1431, 11 1965.
- [48] L. C. Andrews and R. L. Phillips, *Laser Beam Propagation through Random Media*, Second Edition. SPIE Press, 2005.
- [49] R. G. Lane, A. Glindemann, and J. C. Dainty, "Simulations of a Kolmogorov phase screen," *Waves Random Media*, vol. 2, p. 209, Apr. 1992
- [50] L. M. Zhang and F. R. Kschischang, "Staircase codes with 6% to 33% overhead," *J. Lightw. Technol.*, vol. 32, no. 10, pp. 1999–2002, 2014.